MATERIALS SCIENCE

Borophenes made easy

Marc G. Cuxart[1]*, Knud Seufert[1], Valeria Chesnyak[1], Wajahat A. Waqas[1], Anton Robert[2], Marie-Laure Bocquet[2], Georg S. Duesberg[3], Hermann Sachdev[3]*, Willi Auwärter[1]*

To date, the scalable synthesis of elemental two-dimensional materials beyond graphene still remains elusive. Here, we introduce a versatile chemical vapor deposition (CVD) method to grow borophenes, as well as borophene heterostructures, by selectively using diborane originating from traceable byproducts of borazine. Specifically, metallic borophene polymorphs were successfully synthesized on Ir(111) and Cu(111) single-crystal substrates and conjointly with insulating hexagonal boron nitride (*h*BN) to form atomically precise lateral borophene-*h*BN interfaces or vertical van der Waals heterostructures. Thereby, borophene is protected from immediate oxidation by a single *h*BN overlayer. The ability to synthesize high-quality borophenes with large single-crystalline domains in the micrometer scale by a straight-forward CVD approach opens up opportunities for the study of their fundamental properties and for device incorporation.

INTRODUCTION

In recent years, the synthesis of two-dimensional (2D) materials with no naturally occurring layered analogs has opened a new path for property engineering based on the choice of constituent elements and the design of in-plane atomic structures. Among the different synthetic 2D materials, elemental layers stabilized by strong covalent bonds are of particular interest (*1*, *2*). As a prominent member of this family, borophene offers intriguing anisotropic electronic and mechanical properties (*3*–*5*). Preceded by early predictions of flat boron clusters (*6*), theoretical studies have shown that borophene can be stable in different polymorphs (*7*) as consequence of the multicenter bonding configuration of boron that leads to multiple hexagonal-based structures with variable density and periodic distribution of single-boron vacancies (*8*). The predesign and selection of such polymorphs is thus expected to yield control on properties and emerging functionalities (*9*–*11*). Such predictions have spurred experimental efforts to synthesize stable 2D polymorphs of boron, referred to as borophenes.

The synthesis of atomically thin borophenes was achieved by Mannix *et al.* (*12*) and Feng *et al.* (*13*) in 2015 by depositing boron from high-purity solid sources onto the (111) surface of an Ag single-crystal in ultrahigh vacuum (UHV) conditions, i.e., following a physical vapor deposition (PVD) method. This procedure was subsequently applied on other surfaces like Ag(110), Ag(100) (*14*, *15*), Cu(111) (*16*), Au(111) (*17*), and Ir(111) (*18*). Nevertheless, the quality of the produced samples constitutes a bottleneck for nonlocal measurements, essential for the exploration of the unique properties predicted in the highly dynamic field of theoretical endeavors. The difficulty to achieve 2D elemental boron films with large single-crystalline domains of high perfection (with a low content of grain boundaries and defects) by PVD results from the high melting point and high reactivity of elemental boron, impeding the formation of single uniform growth species by thermal evaporation procedures. Compared to mere PVD techniques, single-source CVD precursor routes offer considerable advantages for the production of 2D materials, like scalability and a controlled dosage of gaseous growth species with a defined molecular stoichiometry in a wide pressure regime (*19*, *20*). However, previous attempts using CVD yielded amorphous boron structures, nanotubes, multilayers, and thick layers, including 3D boron structures (*21*–*23*). In addition, high-temperature decomposition of *h*BN gave access to boron monolayers (*24*–*26*). Overall, the lack of a suitable boron precursor that prompts 2D nucleation and growth has been the major impediment to produce atomically thin borophenes.

Derived from previous experience regarding the use of borazine ($B_3N_3H_6$) for *h*BN synthesis (*27*, *28*), we were able to identify diborane (B_2H_6) in commercial borazine. Here, we selectively used diborane as a molecular precursor for the CVD growth of high-quality atomically thin borophene layers and developed an easy and controllable CVD route for (i) extended layers of borophenes on distinct supports and (ii) unprecedented vertical and lateral heterostructures combining borophene with *h*BN (see Fig. 1). The *h*BN cover is shown to prevent degradation of borophene when exposed to oxygen at room temperature. *h*BN encapsulation of sensitive 2D materials (such as metal dichalcogenides, phosphorene, and magic angle graphene bilayers), mostly realized by transfer techniques to date, can protect the material's properties and ease device implementation (*29*–*31*). However, no such passivation of borophene was reported so far, posing challenges for many applications as borophene rapidly oxidizes in air (*32*). An *h*BN protection of borophene, demonstrated by the presented CVD approach, might thus complement recent achievements, yielding ambient-stable borophane by hydrogenation of PVD-grown borophene (*32*), and open pathways to exploit borophene properties in van der Waals heterostructures and devices (*33*).

RESULTS AND DISCUSSION

In the presented CVD method, diborane is dosed onto a preheated, atomically clean, and flat surface under UHV conditions, as schematically illustrated in Fig. 1A, after being selectively filtered from borazine by applying a freeze-thaw cycle with a liquid nitrogen-cold trap in the precursor dosing system. The mass spectrum depicted in Fig. 1I resulting after the cold trap activation shows a signal ranging from 23 to 27 atomic mass unit (amu) attributed to ^{10}B and ^{11}B isotopes

[1]Physics Department E20, Technical University of Munich, James-Franck-Str. 1, 85748 Garching, Germany. [2]PASTEUR, Département de Chimie, École Normale Supérieure, PSL University, Sorbonne Université, CNRS, 75005 Paris, France. [3]Fakultät für Elektrotechnik und Informationstechnik, Institut für Physik EIT-2, Universität der Bundeswehr München, Werner-Heisenberg-Weg 39, D-85579 Neubiberg, Germany.
*Corresponding author. Email: marc.gonzalez-cuxart@tum.de (M.G.C.); wau@tum.de (W.A.); hermann.sachdev@unibw.de (H.S.)

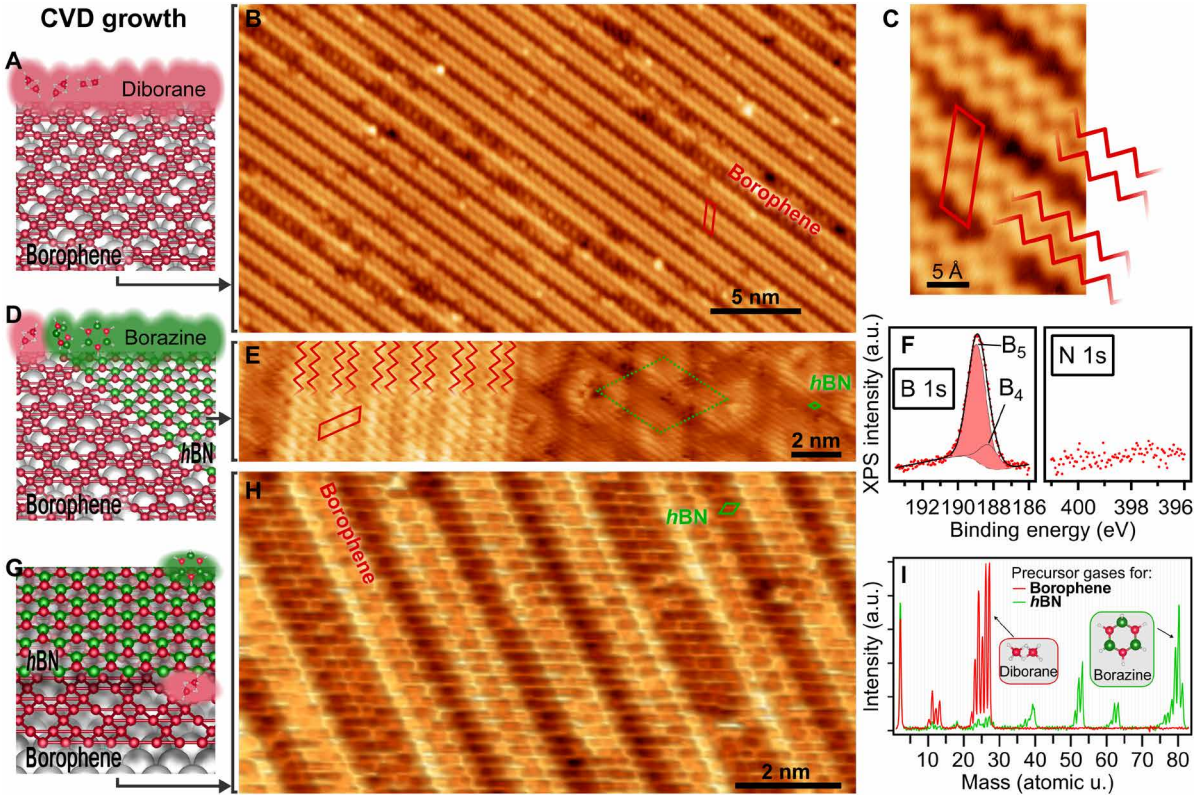

Fig. 1. CVD growth of borophene and borophene-*h*BN heterostructures on Ir(111). (**A**) Schematic of diborane dosage on the preheated Ir(111) surface to obtain borophene. (**B**) STM image of a single-crystalline borophene domain grown by CVD on Ir(111) (V_{bias} = 0.1 V). (**C**) Detailed structure of borophene whose unit cell is depicted in red (V_{bias} = 2.0 V). (**D**) Schematic of sequential borazine and diborane dosage to obtain borophene-*h*BN lateral heterostructures. (**E**) High-resolution STM image of the lateral heterostructure formed by borophene and *h*BN (V_{bias} = 1.2 V). Red lines highlight χ_6 borophene's wavy appearance, and green solid and dashed rhomboids highlight the unit cell and hexagonal moiré pattern of *h*BN, respectively. (**F**) XPS boron and nitrogen 1s core levels measured on borophene. (**G**) Schematic of the vertical heterostructure, with *h*BN covering borophene, grown by sequential dosing. (**H**) Atomically resolved image of the *h*BN lattice covering the borophene in the vertical heterostructure. (V_{bias} = 0.10 V; subtle 3D rendering was applied for better visualization). (**I**) Mass spectra of diborane and borazine gas used to grow borophene and *h*BN, respectively, measured at partial pressure of 3×10^{-7} mbar.

of diborane (and borane BH_3 at 14 amu) and vanishing intensity of masses above 29 amu. In contrast, the mass spectrum of the nonfiltered gas (cold trap deactivated) presents different sets of peaks resulting from the borazine precursor (*34*). Since amine borane (H_3B-NH_3) is one of the major intermediates in borazine syntheses, inseparable byproducts derived from this precursor [e.g. μ-aminodiborane ($B_2H_5NH_2$), polymer aminoboranes (NH_2-BH_2)$_2$ and borane adducts of (oligomer and polymer) amine boranes and aminoboranes [H_3B-(NH_2-BH_2)$_n$-NH_3] can act upon decomposition as an ubiquitous source for diborane (*35*, *36*), together with precursor degradation by mandatory handling issues. Traces of μ-aminodiborane are detectable by ^{11}B-nuclear magnetic resonance spectroscopy in the commercial borazine (see fig. S1). These aspects, together with trace signals in the range of 95 amu found in the used borazine in comparison to those found for a borane-tetrahydrofuran adduct (fig. S2), hint to a weak interaction and adduct formation of borane with neat borazine as per eq. S5 in the Supplementary Materials. Therefore, the presence and continuous reformation of diborane with time is readily explained by an ongoing decay of inherent or acquired trace impurities in the commercial borazine precursor, which is also widely used for *h*BN monolayer synthesis. See fig. S2 for a simple time evolution of diborane in our borazine dosing system.

The resulting material grown after dosing diborane as described above on Ir(111) (kept at 1233 K) was in situ characterized by low-temperature scanning tunneling microscopy (STM) and x-ray photoelectron spectroscopy (XPS). The STM image in Fig. 1B shows a single-crystalline domain of an overlayer with stripy appearance, presenting a "wavy" pattern that is resolved in the high-resolution STM image in Fig. 1C (highlighted in red). This structure can be described by the unit cell depicted in red, with lattice vectors $|\mathbf{a}| = 16.2 \pm 1.0$ Å and $|\mathbf{b}| = 5.4 \pm 1.0$ Å, forming an angle of $\phi = 60°$. Three equivalent rotational single-crystalline domains with large lateral extensions of at least hundreds of nanometers were observed, each of them having the stripes aligned along the $\langle 1\bar{1}0 \rangle$ high-symmetry directions of the underlying surface (figs. S3 and S4). The same structure on Ir(111) was recently identified as a χ_6-like borophene polymorph (with a number of boron vacancies per number of atomic sites of $\eta = 1/6$) (*18*). The wavy appearance emerges as consequence of the threefold commensurate 6×2 stacking with Ir(111). In the reported case, borophene was synthesized by evaporation of elemental boron from a solid source onto the substrate, i.e., by using a PVD method yielding domains of smaller size and higher density of domain boundaries than those obtained here by CVD (*18*).

In the present study, the Ir(111) surface was found to be fully covered by the borophene layer after dosage of 1.8 Langmuir (L), yet

further growth processes performed at higher diborane doses yielded the same complete coverage. This demonstrates the substantial decrease of the growth kinetics after the completion of the first atomic layer and strongly suggests that the molecular precursor undergoes dehydrogenation reactions assisted by the catalytic surface, yielding intermediate boron species that form large single-crystalline domains. Boron subsurface diffusion and segregation mechanisms may not generally be excluded but are not expected to dominate the growth at the applied conditions due to the kinetic differences between on surface film formation and bulk diffusion mechanisms (*16*, *26*, *37*). Low-energy electron diffraction (LEED) imaging reveals successful borophene formation at temperatures as low as 1073 K (fig. S5).

XPS characterization of the borophene polymorph grown by CVD is presented in Fig. 1F, confirming the presence of boron and absence of nitrogen. The B 1s core-level signal consists of a single peak that can be well-described by the sum of two Voigt-like functions (B_5 and B_4) steaming from the two different coordination numbers of B within the borophene layer (*38*). These are centered at binding energies of 188.9 and 188.2 eV, up-shifted with respect to other borophenes on Ag(111) (*13*, *38*) and Cu(111) (*39*). The shift is consistent with a reduced adsorption distance on Ir(111) [2.1 Å (*18*)] compared to Ag(111) [2.4 Å (*13*)] and Cu(111) [2.3 Å (*40*)] and points toward a stronger borophene-substrate interaction for Ir(111), reminiscent of the trend observed for other 2D materials (*41*). On the other hand, the lack of a N 1s signal evidences the absence of *h*BN domains and corroborates the selective growth of borophene.

Thereupon, we address the combined growth of borophene and single-layer *h*BN (referred to as *h*BN), the latter being a multifunctional, insulating 2D material (*42*). Borophene has been only combined with graphene (*43*) and with a molecular assembly formed by perylene-3,4,9,10-tetracarboxylic dianhydride (*44*) to date, although well-defined lateral or vertically stacked heterostructures offer a huge potential for nanodevices (*33*, *45*).

As a first example, borophene-*h*BN lateral heterostructures were synthesized on Ir(111). Taking advantage that diborane and borazine coexist in the same compound, and they can be selectively dosed by activating and deactivating the cold trap, 0.1 L of borazine was dosed onto Ir(111) kept at 1233 K in the first step, followed by 1.8 L of diborane in the second step (as shown schematically in Fig. 1D). The dose of borazine corresponds to submonolayer growth of *h*BN, therefore allowing enough free catalytic surface for borophene formation, in contrast to higher doses leading to a full layer of *h*BN (figs. S6 and S7). The resulting 2D layer reveals coexisting domains of borophene and *h*BN that fully cover the Ir(111) surface, hence forming lateral heterostructures, as shown in Fig. 1E and fig. S8. Borophene domains feature the three orientations and the stripy appearance with wavy motifs discussed above (Fig. 1C), while also *h*BN domains preserve the characteristic appearance reported earlier for pristine *h*BN/Ir(111) (*24*). The latter represents a single 12-on-11 moiré superstructure with a periodicity of 2.89 nm (depicted by a green dashed rhombus in Fig. 1E) (*24*). *h*BN zigzag-terminated edges (and the corresponding *h*BN symmetry axis) are oriented in parallel to the borophene stripes, both aligned to one of the three high-symmetry axis of Ir(111). In addition, borophene edges parallel to the stripes are energetically preferred, as indicated by their prevalence in borophene islands (*18*) and interfaces to *h*BN. This promotes the formation of straight heterojunctions oriented in three equivalent directions with fixed lateral stacking. These straight segments extend over tens of nanometers (fig. S8), in stark contrast to the irregular lateral interfaces formed by borophene and graphene (*43*), highlighting the influence of epitaxy and growth temperature.

The formation of a straight and atomically sharp 1D interface is supported by an atomic-scale description of the bonding configuration based on density functional theory (DFT; see fig. S15). It suggests an *h*BN-borophene 11 × 5 lateral commensurability, in which 10 over 11 interfacial boron atoms form covalent B—B bonds with borophene, while the topographic appearance of both 2D materials is not strongly distorted. This is observed experimentally as shown in the atomically resolved STM image in Fig. 2A and fig. S10 (highlighting the interfacial atomic registry).

The electronic transition from borophene to *h*BN occurs within a distance of ~5 Å, with no apparent interface states, as evidenced by the series of scanning tunneling spectra (STS) recorded across the lateral heterojunction in Fig. 2D and fig. S9. The low-energy electronic structure of borophene is characterized by spectral features near the Fermi level E_F, whose intensities vary laterally, matching the periodicity of the stripe-like topography. The borophene-related density of states extends to the very interface with *h*BN. The spectroscopical features are clearly visualized in the differential conductance (dI/dV) spectrum in Fig. 2B, where a minimum intensity around 0.7 V is observed. While the line shape compares reasonably well with those measured for borophenes χ_3 and β_{12} on Ag(111) (*12*) and χ_3 like on Cu(111), the position of the minimum is observed at higher voltage (see also fig. S9). The linear I(V) spectra (Fig. 2C) confirms the characteristic metallic behavior of borophene also for this polymorph.

At the other side of the interface, *h*BN presents an electronic structure with lower density of states at E_F (Fig. 2, B and D), which is spatially modulated along the moiré pattern as a consequence of the registry-dependent hybridization of N with Ir atoms (*46*). In Fig. 2C, the crossing between dI/dV spectra corresponding to *h*BN "valley" and "rim" regions is consistent with the STM contrast inversion observed at different bias voltages in Fig. 2 (E and F); likewise, the electronic contribution of the *h*BN and borophene represented by the dI/dV curves accounts for the contrast inversion between both 2D layers. The LEED analysis presented in fig. S13 confirms that diborane dosing is essential to achieve the planar heterostructure, i.e., under the applied conditions, borazine dosing alone cannot explain the resulting heterostructures.

As a second example of a borophene-*h*BN heterostructure achieved by the presented CVD method, *h*BN-covered borophene was synthesized by sequentially dosing 1.8 L of diborane and 4.5 L of borazine onto Ir(111) kept at 1223 K (Fig. 1, G and H). Both doses correspond to those required to grow a full monolayer of borophene and *h*BN on Ir(111), respectively. The atomically resolved STM image of the resulting sample in Fig. 3A shows the *h*BN honeycomb structure, with a measured lattice constant of 2.49 Å, slightly modulated along the characteristic parallel stripes of this borophene polymorph presented in Fig. 1B. As expected for a large gap insulator like *h*BN, the atomic lattice can only be imaged under certain tip and scanning conditions, otherwise only the stripy appearance of borophene is observed (see fig. S11), i.e., the *h*BN cover appears "transparent" for STM (*47*). The orientation of the *h*BN on borophene is not unique but consists on a manifold of misalignments around borophene's wavy direction (Figs. 1H and 3A and fig. S11), in contrast to the situation for *h*BN on Ir(111) (see Fig. 1E and fig. S6), indicating a weak interaction between *h*BN and borophene. This is confirmed by LEED data (inset of Fig. 3A), in which the *h*BN

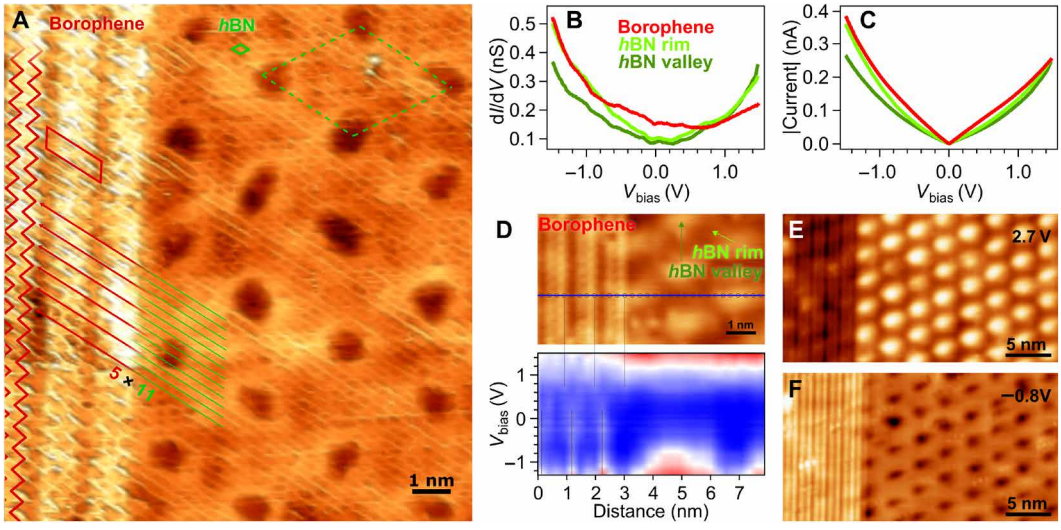

Fig. 2. Borophene-*h*BN lateral interface on Ir(111). (**A**) High-resolution STM image of the atomically sharp heterointerface formed by borophene and *h*BN (V_{bias} = − 0.5 V). Subtle 3D rendering was applied for better visualization. The interfacial registry is highlighted by the red and green lines. (**B**) d*I*/d*V* spectra taken on borophene and *h*BN rim and valley regions, together with (**C**) simultaneously acquired *I*(V) curves (stabilization conditions: V_{bias} = 1.5 V, I_t = 0.25 nA, lock-in modulation voltage *V* = 50 mV). The borophene spectra represent an average over the unit cell. (**D**) d*I*/d*V* intensity map constructed from the series of d*I*/d*V* spectra measured along the blue line marked on the STM image (V_{bias} = 2.0 V) showing a sharp electronic transition. Spectra stabilized at V_{bias} = 1.5 V and I_t = 0.4 nA, lock-in modulation voltage *V* = 50 mV. STM images measured at (**E**) V_{bias} = 2.7 and (**F**) V_{bias} = − 0.8 V, showing a bias-dependent contrast inversion between borophene and *h*BN.

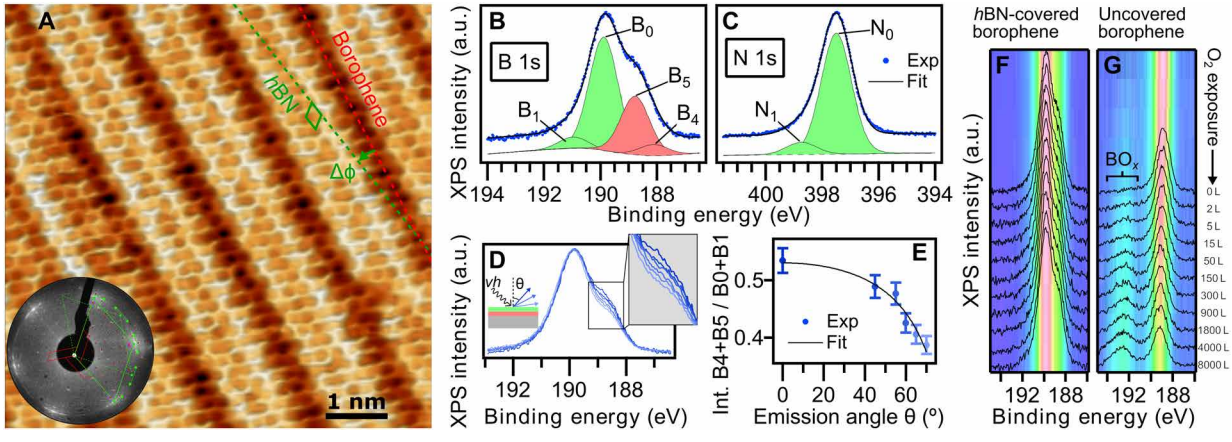

Fig. 3. *h*BN on borophene: vertical heterostructure on Ir(111). (**A**) Atomically resolved STM image of an *h*BN domain, featuring its honeycomb structure, on χ_6 borophene, showing its stripy appearance on Ir(111) (*h*BN unit cell in green, V_{bias} = 1.0 V). Subtle 3D rendering has been applied for better visualization. Inset: LEED pattern acquired at 79 eV (simulated diffraction pattern of *h*BN in green and borophene in red). (**B**) Boron and (**C**) nitrogen 1s XP spectra. The fitted components of *h*BN and borophene spectral contributions are displayed in green and red, respectively. (**D**) B 1s peak measured at different photoelectron emission angles θ = 0°, 45°, 55°, 60°, 65°, and 70° (lines from dark to light blue). (**E**) Angular dependence of the relative intensity of borophene B 1s components and Beer-Lambert law fit in black describing the attenuation effect by the *h*BN overlayer. (**F**) Series of B 1s spectra measured on *h*BN-covered borophene after incremental O_2 exposure intervals reveals no sign of oxidation in contrast to an uncovered borophene sample that shows emergence of oxidized boron (**G**). Intensity maps at the background are constructed with the presented spectra.

diffraction pattern consists on a ring-like structure with local intensity maxima around the main symmetry axis of the Ir(111) diffraction pattern and around rotational angles of 30°, a consequence of the presence of *h*BN rotational domains (see fig. S13). This is in stark contrast to the substrate-locked orientation of *h*BN domains on Ir(111) (see fig. S13 for extended LEED characterization and discussion). In addition, weak diffraction spots corresponding to the borophene 2 × 6 superstructure, attenuated by the *h*BN cover, are observed. The DFT-optimized structure of the vertical interface reveals a planar *h*BN overlayer and shows no modification of the constituent's electronic properties (fig. S16).

The XPS B 1s spectrum of the vertical heterostructure (Fig. 3B) shows a highly asymmetric peak shape that can be deconvoluted in four contributions emerging from B constituting borophene (B_4 and B_5) and *h*BN (B_0 and B_1). Peak fitting was performed by using the borophene components presented in Fig. 1 and reproducing a

two-component structure that models the corrugation-dependent *h*BN-substrate interaction (*41*). The largely dominant intensity of the *h*BN low-energy component B_0 over B_1 (ratio 10:1), characteristic of weakly interacting *h*BN layers with low degree of corrugation, is consistent with the rotational domains and flat *h*BN observed by LEED and STM. The N 1s spectrum in Fig. 3C was accordingly modeled by two components N_0 over N_1 with the same intensity ratio of 10:1. Fit parameters are summarized in table S1. To verify the vertical order of borophene and *h*BN, XPS measurements at different photoelectron emission angles (θ) were conducted (Fig. 3D). The intensity of the borophene B 1s components (normalized by those of *h*BN) observed in Fig. 3E decreases as θ increases. This is attributed to the attenuation effect of the *h*BN cover, as the intensity drop is well described by the Beer-Lambert law (Fig. 3E), and the same effect is not observed in the case of the lateral heterostructure (see fig. S12).

Since oxidation of borophene appears as a major issue limiting its stability when exposed to air, the protective capping effect that inert *h*BN could confer to borophene was assessed. Two series of B 1s XP spectra measured on *h*BN-covered and noncovered borophene, respectively, upon exposure to incremental doses of molecular oxygen (O_2) at room temperature are plotted in Fig. 3 (F and G). For bare borophene, a broad component emerges attributed to boron oxides (*28*) around 192 to 194 eV, at expenses of the main peak that goes in hand with an increase of O 1s (see fig. S14). In contrast, the B 1s peak of the covered borophene in Fig. 3F remains completely unchanged, evidencing that *h*BN acts as a protective layer against O_2 oxidation of borophene in the studied dose range.

Last, we considered the growth of borophene on Cu(111) as a weaker interacting support, to assess the applicability of the CVD method to a wider range of metal substrates. Cu is particularly interesting in view of applications, as a readily accessible material whose typically low interactions with supported 2D materials makes it suitable for different transfer processes to technologically relevant substrates and for scalable fabrication (*48*–*50*). Similar to the CVD procedure described above for the case of Ir(111), 18 L of diborane was dosed onto a Cu(111) single-crystal kept at 773 K. The resulting material was characterized by STM, revealing the presence of single-crystalline domains (Fig. 4A). Even at a low coverage (around 40%, as shown in the inset in Fig. 4A), the domains extend over hundreds of nanometers, which, together with the low density of nucleation sites, suggests that much larger domains can be achieved (*39*). Detailed inspection of the domains by high-resolution STM imaging allows the characterization of their in-plane periodic structure. Albeit presenting distinct appearances at positive and negative bias voltages (Fig. 4, B and C, respectively), the structure can be described by a unit cell with $|\mathbf{a}| = 15.57 \pm 1.0$ Å and $|\mathbf{b}| = 21.5 \pm 1.0$ Å, forming an angle of $\phi = 73^{\circ}$, consistent with the fast Fourier transform shown in the top right inset in Fig. 4A. It leads to the formation of mirror-symmetric domains aligned with the $\langle 1\bar{1}0 \rangle$ high-symmetry directions of Cu(111) (see fig. S17). Structure and STM appearance are in agreement with the χ_3-like borophene polymorph (defined by $\eta = 1/5$) on Cu(111) reported by Wu *et al.* (*16*, *39*) in that case prepared by a PVD method and complemented by postannealing cycles. Thus, deliberately choosing Cu(111) and Ir(111), we have demonstrated that the same structures can be obtained by a different approach, therefore verifying that this CVD method can deliver boron for the generation of borophenes and heterostructures with *h*BN.

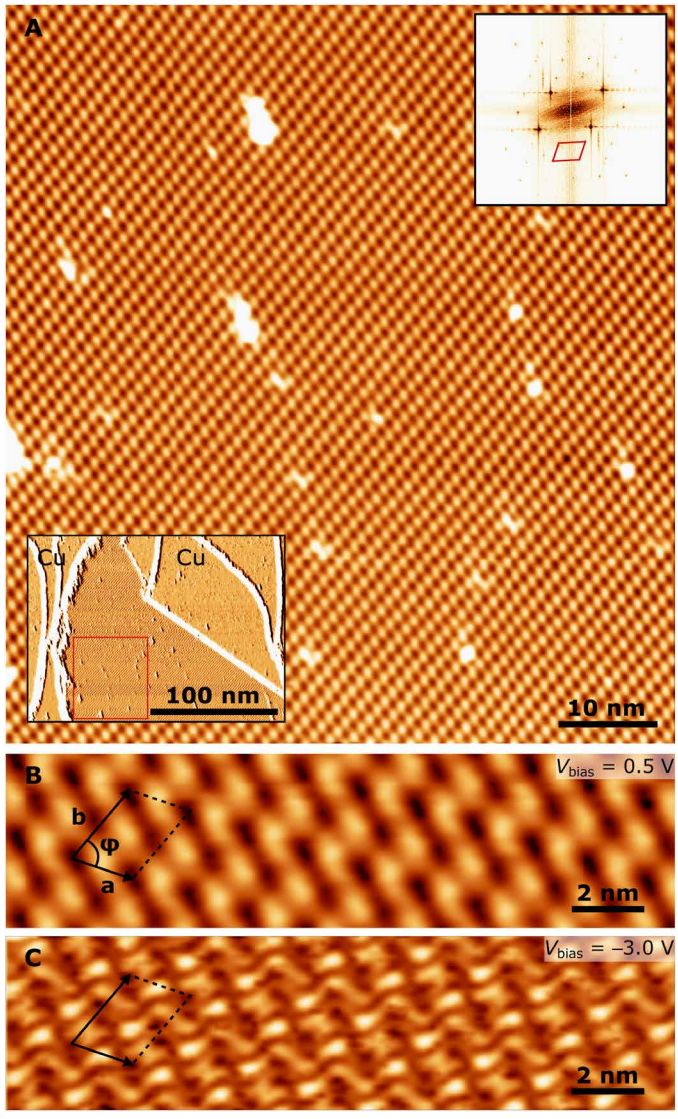

Fig. 4. CVD growth of borophene on Cu(111). (**A**) STM image of a single-crystalline χ_3-like borophene domain (V_{bias} = 1.3 V). Top right inset shows a fast Fourier transform of the image. The scan area is highlighted in the bottom left inset (tunneling current channel, V_{bias} = 1.3 V). (**B** and **C**) High-resolution STM images of the same borophene domain recorded at V_{bias} = 0.5 and −3.0 V, respectively. Black vectors indicate the unit cell.

Our findings demonstrate the feasibility of a CVD route to borophene polymorphs using diborane as boron source. Dosing different CVD precursors from one supply container using the presented technique allows the selective deposition of borophene (from diborane) or *h*BN sheets (from borazine) or combined lateral/vertical heterostructures of borophene and *h*BN. It also stresses the relevance of high purity precursors for the selective deposition of single phases. The anisotropic morphology of borophene domains furthermore enables atomically precise alignment and contacting of other components like it is shown for *h*BN. This versatile method can be used on different substrates and opens pathways for the in situ growth of heterostructures involving low-dimensional materials with complementary properties and for the protection of

borophene from oxidation. The use of diborane, (substituted) boranes, and molecular boron precursors, in general, has the potential to become the long sought-after route toward polymorph-selective and scalable methods for high-quality layers of borophenes, their heteroatom-substituted derivatives, or even for boron- or boride-based materials. This will open a vast variety of approaches to study fundamental aspects of these synthetic 2D materials and finally bring their incorporation in technologically relevant applications into reach. Note added: During evaluation of this manuscript, a study reporting another approach to borophene synthesis on Ir(111) was published (*51*).

MATERIALS AND METHODS

Borophene and borophene heterostructure growth

The Ir(111) and Cu(111) single crystals were prepared by repeated cycles of sputtering (Ar^+ ions at an energy of 1 keV) and resistive annealing at 960° and 760°C, respectively. Borophene was grown on Ir(1111) and Cu(111) by dosing from 1.8 to 4.2 and 18 L of diborane while keeping the substrates at 1233 and 773 K, respectively. Borophene-*h*BN lateral heterostructures were grown sequentially dosing 0.1 L of borazine (cold trap deactivated) and 1.8 L of diborane (cold trap activated) on Ir(111) kept at 1233 K. Borophene-*h*BN vertical heterostructures were grown sequentially dosing 1.8 L of diborane and 4.5 L of borazine on Ir(111) kept at 1233 K. Borazine from a commercial supplier was used (Katchem spol. s.r.o., Prague, Czech Republic, www.katchem.cz/en).

Sample characterization

STM and STS data were acquired by a CreaTec STM operating at 6 K and $P < 2 \times 10^{-10}$ mbar. STM images were taken at constant current mode and processed using the WSxM software (*52*). dI/dV spectra were acquired in constant height mode at $f = 961$ Hz and at the peak-to-peak modulation voltage stated in figure captions. XPS data were taken by a SPECS PHOIBOS 100 hemispherical electron analyzer using the Al K_α line as x-ray source (1253.6 eV) and energy referenced to E_F, calibrated using the energy position of the Ag $3d_{5/2}$ peak measured on a clean Ag(111) single-crystal as a reference. Measurements were performed at room temperature and $P = 1 \times 10^{-9}$ mbar. Fits to the experimental data were performed using the XPST macro for IGOR (M. Schmid, Philipps University Marburg), using Voigt-like functions (Gauss-Lorentzian ratio of 0.1). The CreaTec STM and SPECS XPS apparatus are mounted in different UHV chambers. Samples were transferred between the CreaTec STM and SPECS XPS setups using a Ferrovac VSN40S UHV suitcase ($P = 1 \times 10^{-9}$ mbar). Mass spectra were measured by a Residual Gas Analyzer 300 from Stanford Research Systems. Further information about precursors characterization and computational methods can be found in the supplementary materials.

SUPPLEMENTARY MATERIALS

Supplementary material for this article is available at https://science.org/doi/10.1126/sciadv.abk1490

REFERENCES AND NOTES

1. A. J. Mannix, B. Kiraly, M. C. Hersam, N. P. Guisinger, Synthesis and chemistry of elemental 2D materials. *Nat. Rev. Chem.* **1**, 0014 (2017).
2. A. Molle, J. Goldberger, M. Houssa, Y. Xu, S.-C. Zhang, D. Akinwande, Buckled two-dimensional Xene sheets. *Nat. Mater.* **16**, 163–169 (2017).
3. A. J. Mannix, Z. Zhang, N. P. Guisinger, B. I. Yakobson, M. C. Hersam, Borophene as a prototype for synthetic 2D materials development. *Nat. Nanotechnol.* **13**, 444–450 (2018).
4. B. Feng, J. Zhang, S. Ito, M. Arita, C. Cheng, L. Chen, K. Wu, F. Komori, O. Sugino, K. Miyamoto, T. Okuda, S. Meng, I. Matsuda, Discovery of 2D anisotropic Dirac cones. *Adv. Mater.* **30**, 1704025 (2018).
5. Z. Zhang, Y. Yang, E. S. Penev, B. I. Yakobson, Elasticity, flexibility, and ideal strength of borophenes. *Adv. Func. Mat.* **27**, 1605059 (2017).
6. I. Boustani, Systematic ab initio investigation of bare boron clusters: Determination of the geometry and electronic structures of B_n (n=2–14). *Phys. Rev. B* **55**, 16426–16438 (1997).
7. Z. Zhang, Y. Yang, G. Gao, B. I. Yakobson, Two-dimensional boron monolayers mediated by metal substrates. *Angew. Chem. Int. Edit.* **54**, 13022–13026 (2015).
8. H. Sachdev, Disclosing boron's thinnest side. *Science* **350**, 1468–1469 (2015).
9. X. Yang, Y. Ding, J. Ni, Ab initio prediction of stable boron sheets and boron nanotubes: Structure, stability, and electronic properties. *Phys. Rev. B* **77**, 041402 (2008).
10. X. Wu, J. Dai, Y. Zhao, Z. Zhuo, J. Yang, X. C. Zeng, Two-dimensional boron monolayer sheets. *ACS Nano* **6**, 7443–7453 (2012).
11. Y. Huang, S. N. Shirodkar, B. I. Yakobson, Two-dimensional boron polymorphs for visible range plasmonics: A first-principles exploration. *J. Am. Chem. Soc.* **139**, 17181–17185 (2017).
12. A. J. Mannix, X.-F. Zhou, B. Kiraly, J. D. Wood, D. Alducin, B. D. Myers, X. Liu, B. L. Fisher, U. Santiago, J. R. Guest, M. J. Yacaman, A. Ponce, A. R. Oganov, M. C. Hersam, N. P. Guisinger, Synthesis of borophenes: Anisotropic, two-dimensional boron polymorphs. *Science* **350**, 1513–1516 (2015).
13. B. Feng, J. Zhang, Q. Zhong, W. Li, S. Li, H. Li, P. Cheng, S. Meng, L. Chen, K. Wu, Experimental realization of two-dimensional boron sheets. *Nat. Chem.* **8**, 563–568 (2016).
14. Q. Zhong, L. Kong, J. Gou, W. Li, S. Sheng, S. Yang, P. Cheng, H. Li, K. Wu, L. Chen, Synthesis of borophene nanoribbons on Ag(110) surface. *Phys. Rev. Mat.* **1**, 021001 (2017).
15. Y. Wang, L. Kong, C. Chen, P. Cheng, B. Feng, K. Wu, L. Chen, Realization of regular-mixed quasi-1D borophene chains with long-range order. *Adv. Mater.* **32**, 2005128 (2020).
16. R. Wu, A. Gozar, I. Božović, Large-area borophene sheets on sacrificial Cu(111) films promoted by recrystallization from subsurface boron. *npj Quantum Mater.* **4**, 40 (2019).
17. B. Kiraly, X. Liu, L. Wang, Z. Zhang, A. J. Mannix, B. L. Fisher, B. I. Yakobson, M. C. Hersam, N. P. Guisinger, Borophene synthesis on Au(111). *ACS Nano* **13**, 3816–3822 (2019).
18. N. A. Vinogradov, A. Lyalin, T. Taketsugu, A. S. Vinogradov, A. Preobrajenski, Single-phase borophene on Ir(111): Formation, structure, and decoupling from the support. *ACS Nano* **13**, 14511–14518 (2019).
19. A. Reina, X. Jia, J. Ho, D. Nezich, H. Son, V. Bulovic, M. S. Dresselhaus, J. Kong, Large area, few-layer graphene films on arbitrary substrates by chemical vapor deposition. *Nano Lett.* **9**, 30–35 (2009).
20. Z. Cai, B. Liu, X. Zou, H.-M. Cheng, Chemical vapor deposition growth and applications of two-dimensional materials and their heterostructures. *Chem. Rev.* **118**, 6091–6133 (2018).
21. J. Tian, Z. Xu, C. Shen, F. Liu, N. Xu, H.-J. Gao, One-dimensional boron nanostructures: Prediction, synthesis, characterizations, and applications. *Nanoscale* **2**, 1375–1389 (2010).
22. G. Tai, T. Hu, Y. Zhou, X. Wang, J. Kong, T. Zeng, Y. You, Q. Wang, Synthesis of atomically thin boron films on copper foils. *Angew. Chem. Int. Edit.* **54**, 15473–15477 (2015).
23. A. Mazaheri, M. Javadi, Y. Abdi, Chemical vapor deposition of two-dimensional boron sheets by thermal decomposition of diborane. *ACS Appl. Mater. Inter.* **13**, 8844–8850 (2021).
24. F. H. Farwick zum Hagen, D. M. Zimmermann, C. C. Silva, C. Schlueter, N. Atodiresei, W. Jolie, A. J. Martínez-Galera, D. Dombrowski, U. A. Schröder, M. Will, P. Lazić, V. Caciuc, S. Blügel, T.-L. Lee, T. Michely, C. Busse, Structure and growth of hexagonal boron nitride on Ir(111). *ACS Nano* **10**, 11012–11026 (2016).
25. M. P. Allan, S. Berner, M. Corso, T. Greber, J. Osterwalder, Tunable self-assembly of one-dimensional nanostructures with orthogonal directions. *Nanoscale Res. Lett.* **2**, 94–99 (2007).
26. M. Petrović, U. Hagemann, M. Horn-von Hoegen, F.-J. Meyer zu Heringdorf, Microanalysis of single-layer hexagonal boron nitride islands on Ir(111). *Appl. Surf. Sci.* **420**, 504–510 (2017).
27. M. Corso, W. Auwärter, M. Muntwiler, A. Tamai, T. Greber, J. Osterwalder, Boron nitride nanomesh. *Science* **303**, 217–220 (2004).
28. H. Sachdev, F. Müller, S. Hüfner, BN analogues of graphene: On the formation mechanism of boronitrene layers—Solids with extreme structural anisotropy. *Diam. Rel. Mater.* **19**, 1027–1033 (2010).
29. S. Ahn, G. Kim, P. K. Nayak, S. I. Yoon, H. Lim, H.-J. Shin, H. S. Shin, Prevention of transition metal dichalcogenide photodegradation by encapsulation with h-BN layers. *ACS Nano* **10**, 8973–8979 (2016).

30. L. Li, J. Kim, C. Jin, G. J. Ye, D. Y. Qiu, F. H. da Jornada, Z. Shi, L. Chen, Z. Zhang, F. Yang, K. Watanabe, T. Taniguchi, W. Ren, S. G. Louie, X. H. Chen, Y. Zhang, F. Wang, Direct observation of the layer-dependent electronic structure in phosphorene. *Nat. Nanotechnol.* **12**, 21–25 (2017).
31. Y. Cao, V. Fatemi, S. Fang, K. Watanabe, T. Taniguchi, E. Kaxiras, P. Jarillo-Herrero, Unconventional superconductivity in magic-angle graphene superlattices. *Nature* **556**, 43–50 (2018).
32. Q. Li, V. S. C. Kolluru, M. S. Rahn, E. Schwenker, S. Li, R. G. Hennig, P. Darancet, M. K. Y. Chan, M. C. Hersam, Synthesis of borophane polymorphs through hydrogenation of borophene. *Science* **371**, 1143–1148 (2021).
33. Y. Liu, N. O. Weiss, X. Duan, H.-C. Cheng, Y. Huang, X. Duan, Van der waals heterostructures and devices. *Nat. Rev. Mater.* **1**, 16042 (2016).
34. R. G. Wilson, Ion mass spectrum of borazine ($B_3N_3H_6$). *J. Appl. Phys.* **44**, 5056–5060 (1973).
35. V. Babenko, G. Lane, A. A. Koos, A. T. Murdock, K. So, J. Britton, S. S. Meysami, J. Moffat, N. Grobert, Time dependent decomposition of ammonia borane for the controlled production of 2D hexagonal boron nitride. *Sci. Rep.* **7**, 14297 (2017).
36. T. Wideman, L. G. Sneddon, Convenient procedures for the laboratory preparation of borazine. *Inorg. Chem.* **34**, 1002–1003 (1995).
37. F. Müller, S. Hüfner, H. Sachdev, S. Gsell, M. Schreck, Epitaxial growth of hexagonal boron nitride monolayers by a three-step boration-oxidation-nitration process. *Phys. Rev. B* **82**, 075405 (2010).
38. G. P. Campbell, A. J. Mannix, J. D. Emery, T.-L. Lee, N. P. Guisinger, M. C. Hersam, M. J. Bedzyk, Resolving the chemically discrete structure of synthetic borophene polymorphs. *Nano Lett.* **18**, 2816–2821 (2018).
39. R. Wu, I. K. Drozdov, S. Eltinge, P. Zahl, S. Ismail-Beigi, I. Božović, A. Gozar, Large-area single-crystal sheets of borophene on Cu(111) surfaces. *Nat. Nanotechnol.* **14**, 44–49 (2019).
40. Y. Liu, E. S. Penev, B. I. Yakobson, Probing the synthesis of two-dimensional boron by first-principles computations. *Angew. Chem. Int. Edit.* **52**, 3156–3159 (2013).
41. A. B. Preobrajenski, M. A. Nesterov, M. L. Ng, A. S. Vinogradov, N. Mårtensson, Monolayer h-BN on lattice-mismatched metal surfaces: On the formation of the nanomesh. *Chem. Phys. Lett.* **446**, 119–123 (2007).
42. W. Auwärter, Hexagonal boron nitride monolayers on metal supports: Versatile templates for atoms, molecules and nanostructures. *Surf. Sci. Rep.* **74**, 1–95 (2019).
43. X. Liu, M. C. Hersam, Borophene-graphene heterostructures. *Sci. Adv.* **5**, eaax6444 (2019).
44. X. Liu, Z. Wei, I. Balla, A. J. Mannix, N. P. Guisinger, E. Luijten, M. C. Hersam, Self-assembly of electronically abrupt borophene/organic lateral heterostructures. *Sci. Adv.* **3**, e1602356 (2017).
45. M. P. Levendorf, C.-J. Kim, L. Brown, P. Y. Huang, R. W. Havener, D. A. Muller, J. Park, Graphene and boron nitride lateral heterostructures for atomically thin circuitry. *Nature* **488**, 627–632 (2012).
46. F. Schulz, R. Drost, S. K. Hämäläinen, T. Demonchaux, A. P. Seitsonen, P. Liljeroth, Epitaxial hexagonal boron nitride on Ir(111): A work function template. *Phys. Rev. B* **89**, 235429 (2014).
47. J. Ducke, A. Riss, A. Pérez Paz, K. Seufert, M. Schwarz, M. Garnica, A. Rubio, W. Auwärter, Layered insulator/molecule/metal heterostructures with molecular functionality through porphyrin intercalation. *ACS Nano* **12**, 2677–2684 (2018).
48. X. Li, W. Cai, J. An, S. Kim, J. Nah, D. Yang, R. Piner, A. Velamakanni, I. Jung, E. Tutuc, S. K. Banerjee, L. Colombo, R. S. Ruoff, Large-area synthesis of high-quality and uniform graphene films on copper foils. *Science* **324**, 1312–1314 (2009).
49. L. Tao, J. Lee, M. Holt, H. Chou, S. J. McDonnell, D. A. Ferrer, M. G. Babenco, R. M. Wallace, S. K. Banerjee, R. S. Ruoff, D. Akinwande, Uniform wafer-scale chemical vapor deposition of graphene on evaporated Cu (111) film with quality comparable to exfoliated monolayer. *J. Phys. Chem. C* **116**, 24068–24074 (2012).
50. T.-A. Chen, C.-P. Chuu, C.-C. Tseng, C.-K. Wen, H.-S. P. Wong, S. Pan, R. Li, T.-A. Chao, W.-C. Chueh, Y. Zhang, Q. Fu, B. I. Yakobson, W.-H. Chang, L.-J. Li, Wafer-scale single-crystal hexagonal boron nitride monolayers on Cu (111). *Nature* **579**, 219–223 (2020).
51. K. M. Omambac, M. Petrović, P. Bampoulis, C. Brand, M. A. Kriegel, P. Dreher, D. Janoschka, U. Hagemann, N. Hartmann, P. Valerius, T. Michely, F. J. Meyer zu Heringdorf, M. Horn-von Hoegen, Segregation-enhanced epitaxy of borophene on Ir(111) by thermal decomposition of borazine. *ACS Nano* **15**, 7421–7429 (2021).
52. I. Horcas, R. Fernández, J. M. Gómez-Rodríguez, J. Colchero, J. Gómez-Herrero, A. M. Baro, WSXM: A software for scanning probe microscopy and a tool for nanotechnology. *Rev. Sci. Instrum.* **78**, 013705 (2007).
53. J.-s. Li, C.-r. Zhang, B. Li, F. Cao, S.-q. Wang, An investigation on the synthesis of borazine. *Inorg. Chim. Acta* **366**, 173–176 (2011).
54. R. F. Porter, J. J. Solomon, Chemical ionization mass spectrometry of borazine. *J. Am. Chem. Soc.* **93**, 56–61 (1971).
55. W. J. Shaw, J. C. Linehan, N. K. Szymczak, D. J. Heldebrant, C. Yonker, D. M. Camaioni, R. T. Baker, T. Autrey, In situ multinuclear NMR spectroscopic studies of the thermal decomposition of ammonia borane in solution. *Angew. Chem. Int. Edit.* **47**, 7493–7496 (2008).
56. H. I. Schlesinger, D. M. Ritter, A. B. Burg, Hydrides of boron. X. The preparation and preliminary study of the new compound B_2H_7N. *J. Am. Chem. Soc.* **60**, 2297–2300 (1938).
57. X. Chen, J.-C. Zhao, S. G. Shore, Facile synthesis of aminodiborane and inorganic butane analogue $NH_3BH_2NH_2BH_3$. *J. Am. Chem. Soc.* **132**, 10658–10659 (2010).
58. H. Nöth, B. Wrackmeyer, *NMR-Basic Principles and Progress, NMR Spectroscopy of Boron Compounds* (Springer Verlag, 1978).
59. A. B. Preobrajenski, M. L. Ng, A. S. Vinogradov, N. Mårtensson, Controlling graphene corrugation on lattice-mismatched substrates. *Phys. Rev. B* **78**, 073401 (2008).
60. K. E. F. Hermann, M. A. H. Van Hove, *LEEDpat* (2014).
61. P. E. Blöchl, Projector augmented-wave method. *Phys. Rev. B* **50**, 17953–17979 (1994).
62. J. P. Perdew, K. Burke, M. Ernzerhof, Generalized gradient approximation made simple. *Phys. Rev. Lett.* **77**, 3865–3868 (1996).
63. G. Kresse, J. Furthmüller, Efficient iterative schemes for ab initio total-energy calculations using a plane-wave basis set. *Phys. Rev. B* **54**, 11169–11186 (1996).
64. A. V. Krukau, O. A. Vydrov, A. F. Izmaylov, G. E. Scuseria, Influence of the exchange screening parameter on the performance of screened hybrid functionals. *J. Chem. Phys.* **125**, 224106 (2006).
65. S. Grimme, J. Antony, S. Ehrlich, H. Krieg, A consistent and accurate ab initio parametrization of density functional dispersion correction (DFT-D) for the 94 elements H-Pu. *J. Chem. Phys.* **132**, 154104 (2010).
66. D. Palmer, *CrystalMaker* (2014).

Acknowledgments

Funding: This work was financially supported by the ERC Consolidator Grant NanoSurfs (no. 615233). M.G.C. acknowledges funding from the European Union's Horizon 2020 Research and Innovation Programme under the Marie Skłodowska-Curie grant agreement no. 892725 (WHITEMAG project). W.A. acknowledges funding by the Deutsche Forschungsgemeinschaft (DFG) via a Heisenberg professorship and support by the Munich Center for Quantum Science and Technology (MCQST) funded by the DFG under Germany's Excellence Strategy–EXC-2111–390814868. The simulation work was granted access to the French HPC resources of TGCC and CINES under grant A7-A0070807364 by GENCI. A.R. acknowledges funding from the EU H2020 Framework Programme/ERC Advanced Grant agreement number 785911-Shadoks. H.S. and G.S.D. acknowledge the European Commission under the projects QUEFORMAL (829035) and Graphene Flagship (881603). **Author contributions:** M.G.C., H.S., and W.A. conceived the study. M.G.C. carried out the experiments with support from K.S., V.C., and W.A.W. H.S. analyzed the precursors chemistry. M.G.C. and H.S. analyzed the data. A.R. and M.-L.B. conducted the calculations. W.A. and G.S.D. developed infrastructure. M.G.C., W.A., and H.S. wrote the manuscript with feedback from all other authors. **Competing interests:** M.G.C., K.S., V.C., G.S.D., H.S., and W.A. are inventors on pending patent application 102021201219.1 submitted to the Deutsches Patent- und Markenamt on 9 February 2021. The authors declare that they have no other competing interests. **Data and materials availability:** All data needed to evaluate the conclusions in the paper are present in the paper and/or the Supplementary Materials.

Submitted 24 June 2021
Accepted 15 September 2021
Published 3 November 2021
10.1126/sciadv.abk1490